A hydrolytically stable Ce(IV) complex of glutarimide-dioxime

Qiaomu Yang,[a] Yusen Qiao,[a] Alex McSkimming,[a] Liane M. Moreau,[b] Thibault Cheisson,[a] Corwin H. Booth,[b] Ekaterina Lapsheva,[a] Patrick J. Carroll,[a] Eric J. Schelter*[a]

[a] P. Roy and Diana T. Vagelos Laboratories, Department of Chemistry, University of Pennsylvania, Philadelphia, PA 19104, United States

[b] Chemical Sciences Division, Lawerence Berkeley National Laboratory, Berkeley, CA 94708 USA.

Phone: (+1)-(215)-898-8633

* e-mail: schelter@sas.upenn.edu

Supporting information

Experimental Procedures

UV-Visible absorption spectroscopy

10 mm pathlength quartz cells were used to contain samples for UV-vis characterizations. Electronic absorption spectra (UV-Vis) were collected on a Perkin Elmer 950 UVVis/NIR spectrophotometer. Deconvolution of the spectra was accomplished with Gaussian functions using fityk.

X-ray crystallography

X-ray intensity data were collected on a Bruker APEXII CCD area detector or a Bruker APEXIII D8QUEST CMOS area detector, both employing graphite-monochromated Mo Kα radiation (λ= 0.71073 Å) at 100(1) K. Rotation frames were integrated using SAINT,[1] producing a listing of unaveraged F2 and σ(F2) values which were then passed to the SHELXT[1] program package for further processing and structure solution. The intensity data were corrected for Lorentz and polarization effects and for absorption using SADABS[2] or TWINABS.[3] Refinement was performed by full-matrix least squares based on F2 using SHELXL.[4] All of the reflections were used during refinement. NonS3 hydrogen atoms were refined anisotropically and hydrogen atoms were refined using a riding model.

Electrochemistry

Voltammetry experiments were performed using a CH Instrument 620D Electrochemical Analyzer/Workstation, and the data were processed using CHI software v9.24. Experiments were performed at benchtop using electrochemical cells that consisted of a 4 mL vial, glassy carbon working electrode, a platinum wire counter electrode, and a silver wire plated with AgCl as a quasi-reference electrode. The quasi-reference electrode was prepared by dipping a length of silver wire in concentrated hydrochloric acid. The working electrode surfaces were polished prior to each set of experiments.

The solution employed during the electrochemistry study was ~3 mM in analyte and 100 mM in NaCl in 2 mL of $CH_3CN{:}H_2O$ (4:1, v/v) or ~3 mM in analyte and 100 mM in $[N^nBu_4][PF_6]$ in 2 mL of propylene carbonate. All data were collected in a positive-feedback IR compensation mode. At the end of the run, ferrocene was added as internal standard for calibration. The potential of the analyte was reported versus ferrocene. The difference in potential under the conditions used was determined in an independent measurement.

DFT calculation

Gaussian 09 Rev. A.02 was used for all electronic structure calculations.[5] The calculation was carried out in Comet cluster from the XSEDE system. A 28-electron small core pseudopotential on cerium with published segmented natural orbital basis set incorporating quasi-relativistic effects, and different functionals and basis sets have been used. Details are described *vide infra*.

X-ray crystallography data

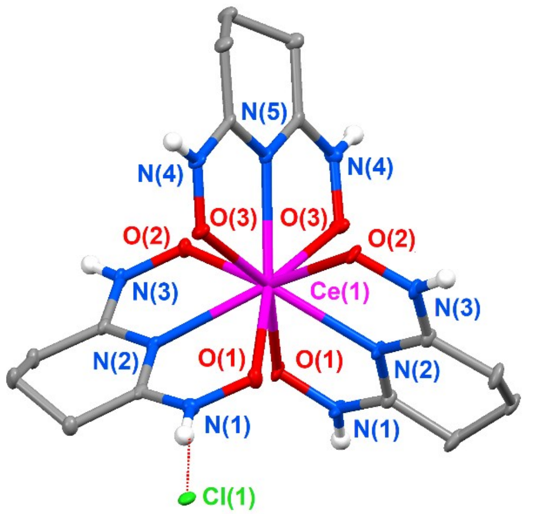

Figure S1. Thermal ellipsoid plot of $[Ce(H_2A)_3]Cl$ at 50% probability (aliphatic proton and H_2O molecules have been omitted for clarity).

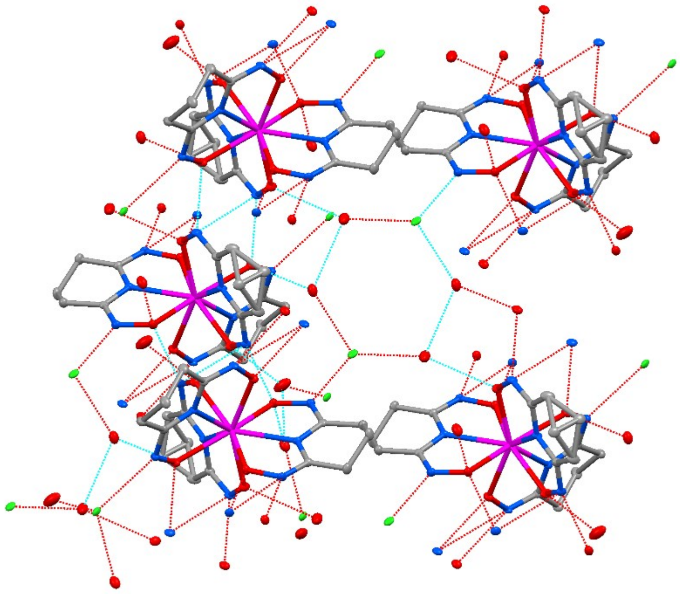

Figure S2. The $[Ce(H_2A)_3]Cl$ molecules form a three-dimensional hydrogen bonding network between individual complexes, Cl^- ions and H_2O molecules.

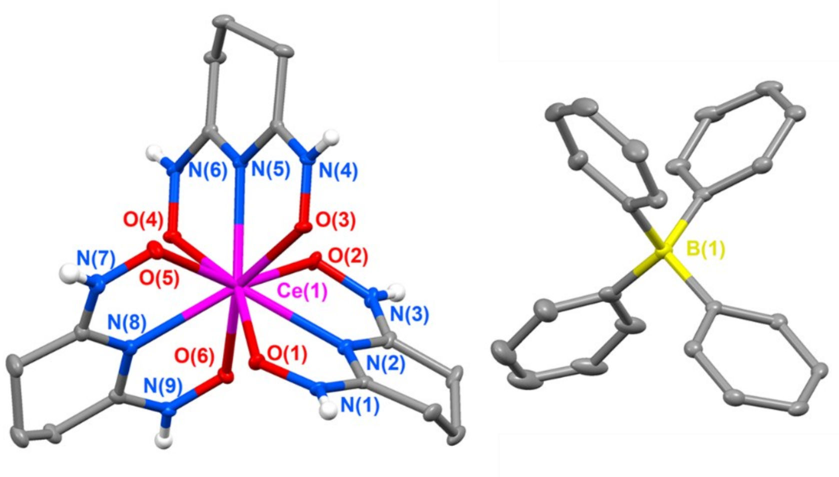

Figure S3. Thermal ellipsoid plot of $[Ce(H_2A)_3][BPh_4]$ (aliphatic protons, aromatic protons and H_2O molecules have been omitted for clarity).

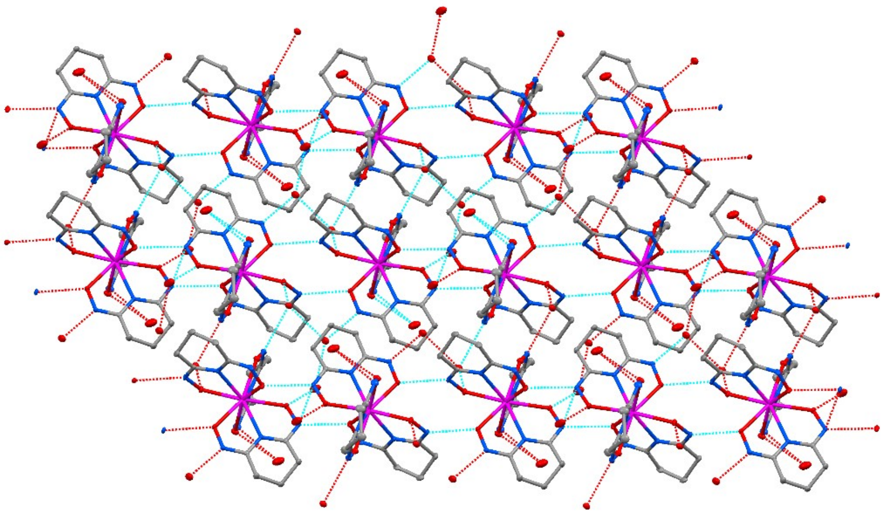

Figure S4. Partial depiction of the crystalline packing of $[Ce(H_2A)_3][BPh_4]$. The overall packing includes $[Ce(H_2A)_3]^+$ fragments that form 2D layers stabilized by hydrogen bonding interactions between complexes and with interstitial water, as indicated by the light blue lines above. The $[BPh_4]^-$ anions form a second 2D layer (not shown).

Table S1. Comparison of distances. M stands for metal (M = Ce, Th, Np). $[Ce^{IV}(H_2A)_3]^+$, $[Th^{IV}(H_2A)_3]^+$, $[Np^{IV}(H_2A)_3]^+$ have similar structures with 3 ligands coordinated to the metal cations in a tridentate fashion. Due to crystal radii differences: Pu 1.1 Å < Ce 1.11 Å < Np 1.12 Å < Th 1.19 Å (taking +4 oxidation state and VIII coordination mode crystal radius for example), there are differences between M-O/N distances. (Pu <= Ce < Np < Th).[6-7]

Species	**$[Ce^{IV}(H_2A)_3]Cl$**	**$[Ce^{IV}(H_2A)_3][BPh_4]$**	**$[Np^{IV}(H_2A)_3]^+$**	**$[Th^{IV}(H_2A)_3]^+$**	**$[Pu^{IV}(H_2A)_3]^+$**
M-O	2.369(4)-2.404(4)	2.3581(10)-2.4157(10)	2.39-2.41	2.44-2.45	2.36-2.40
M-N	2.470(6)-2.487(5)	2.4774(12)-2.4899(12)	2.48-2.50	2.54-2.56	2.45-2.47
O-N	1.367(6)-1.377(6)	1.3575(15)-1.3733(15)	1.37-1.38	1.36-1.38	1.36-1.38
C-N	1.343(6)-1.353(7)	1.3471(19)-1.3542(18)	1.35-1.36	1.33-1.35	1.33-1.35
C=N	1.295(7)-1.302(7)	1.2968(19)-1.302(2)	1.30-1.31	1.29-1.32	1.29-1.30

^{1}H and ^{13}C NMR spectra

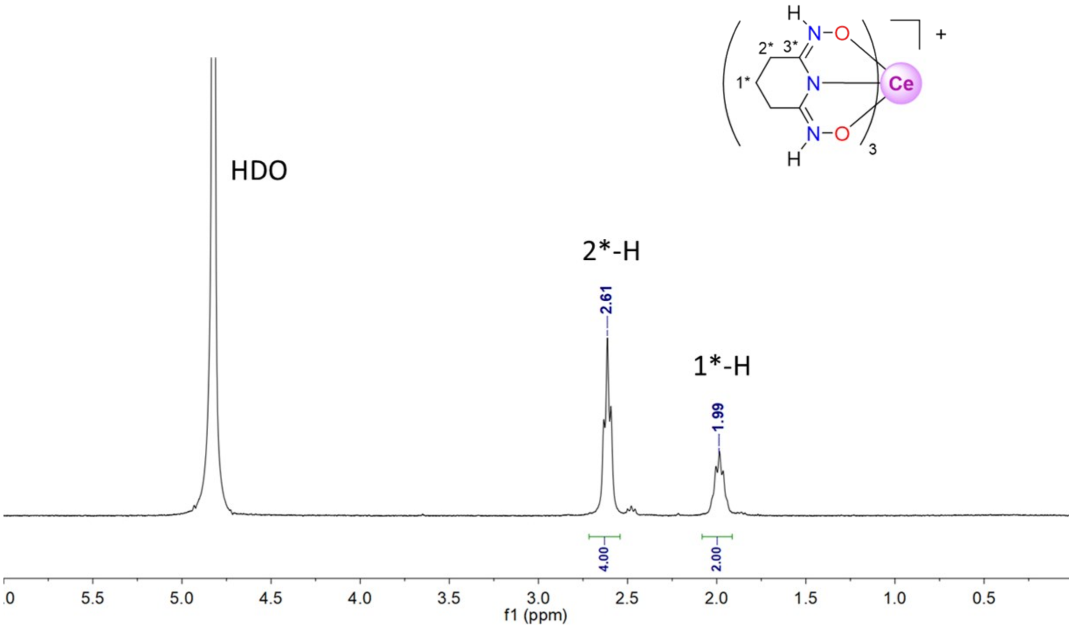

Figure S5. ^{1}H NMR spectrum for $[Ce(H_2A)_3]Cl$ in D_2O (300 MHz, room temperature). Chemical shifts were indicated in the figure.

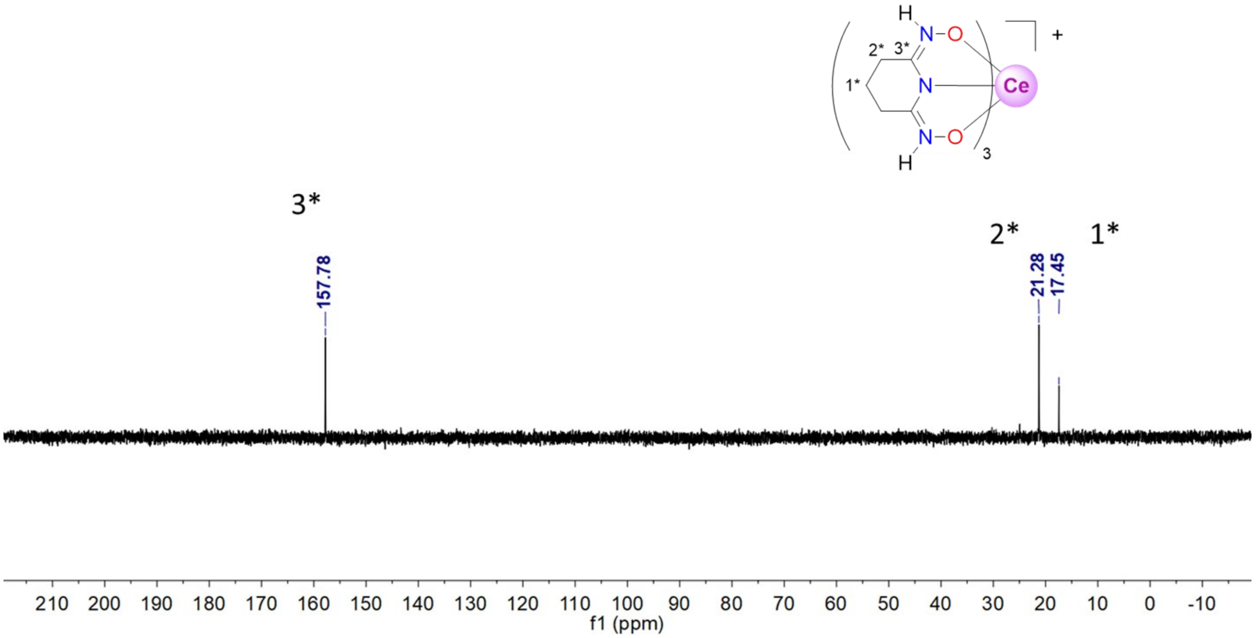

Figure S6. ^{13}C NMR spectrum for $[Ce(H_2A)_3]Cl$ in D_2O (126 MHz, room temperature). Chemical shifts were indicated in the figure.

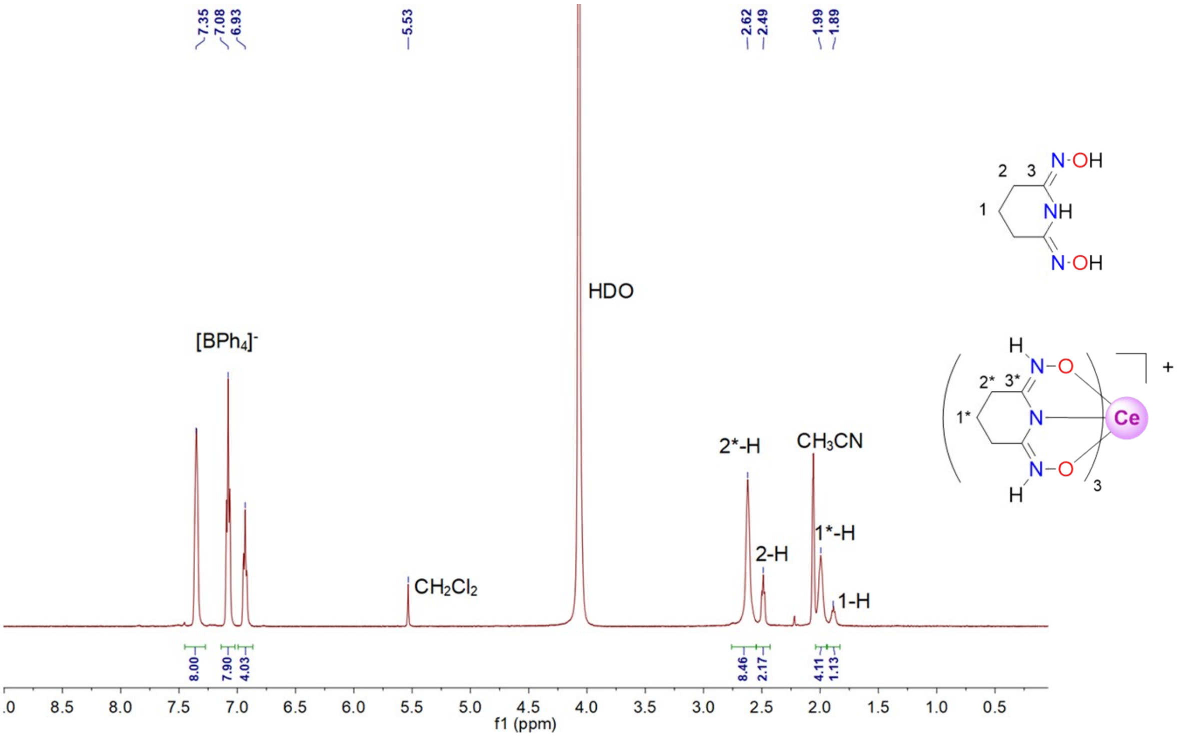

Figure S7. ^{1}H NMR spectrum for $[Ce(H_2A)_3][BPh_4]$ in CD_3CN-D_2O (2:1, 300 MHz, room temperature). Chemical shifts were indicated in the figure.

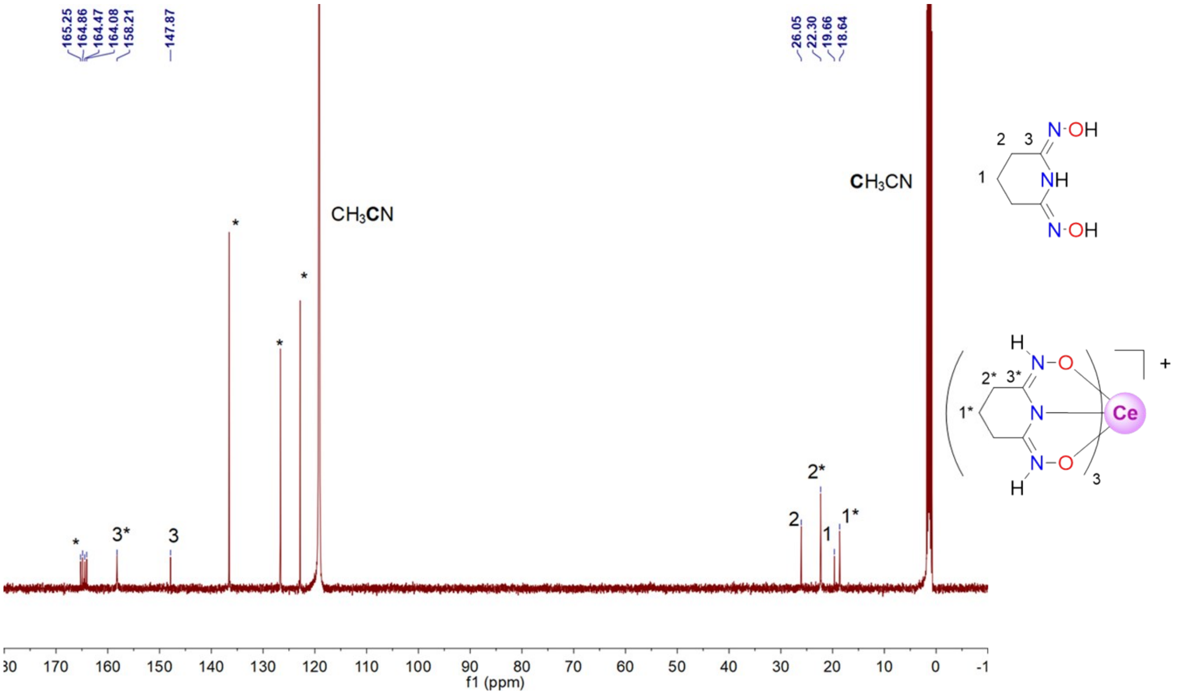

Figure S8. ^{13}C NMR spectrum for $[Ce(H_2A)_3][BPh_4]$ in CD_3CN-D_2O, * indicates peaks for $[BPh_4]^-$ (126 MHz, room temperature). Chemical shifts were indicated in the figure.

Notably, $[Ce(H_2A)_3][BPh_4]$ showed both H_3A and $[Ce(H_2A)_3]^+$ signals in an acetonitrile-water solution mixture. The dissociation of H_2A^- ligand from $[Ce(H_2A)_3]^+$ was likely solvent dependent. This observation may indicate that the presence of acetonitrile promotes H_2A^- ligand dissociation. Acetonitrile is a less polar solvent with smaller dielectric constants compared with water, and it does not engage in appreciable hydrogen bonding. Considering that the charges within the oxime arms of the glutarimide-dioxime ligand become zwitterionic upon coordination to the cerium(IV) (scheme S1). The hydrogen-bonded water presumably stabilizes the zwitterionic form of the glutarimide-dioxime ligand. Addition of acetonitrile is expected to disrupt hydrogen bonding of water with the zwitterionic ligand, and result in a more labile interaction of the H_2A^- ligand from the $[Ce(H_2A)_3]^+$ complex.

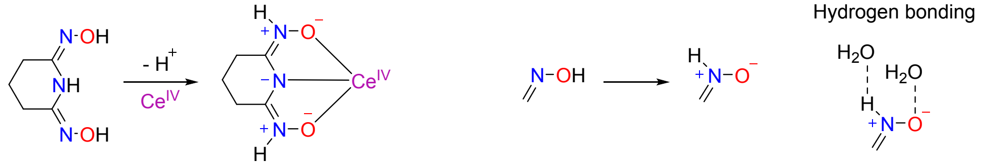

Scheme S1. Schematic diagram for the transformation of neutral oxime arm from glutarimide-dioxime into a zwitterion. The resulting zwitterion favors hydrogen bonding with solvents.

UV-Vis data

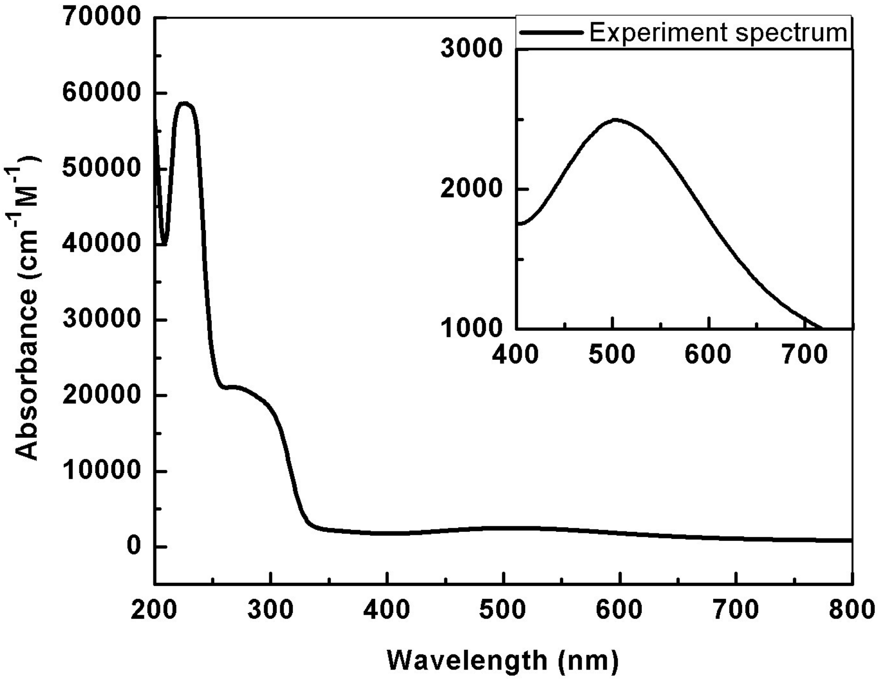

Figure S9. Original UV-Vis spectrum of [Ce(H_2A)$_3$]Cl in H_2O. The full spectrum was recorded on a 0.0452 mM aqueous solution.

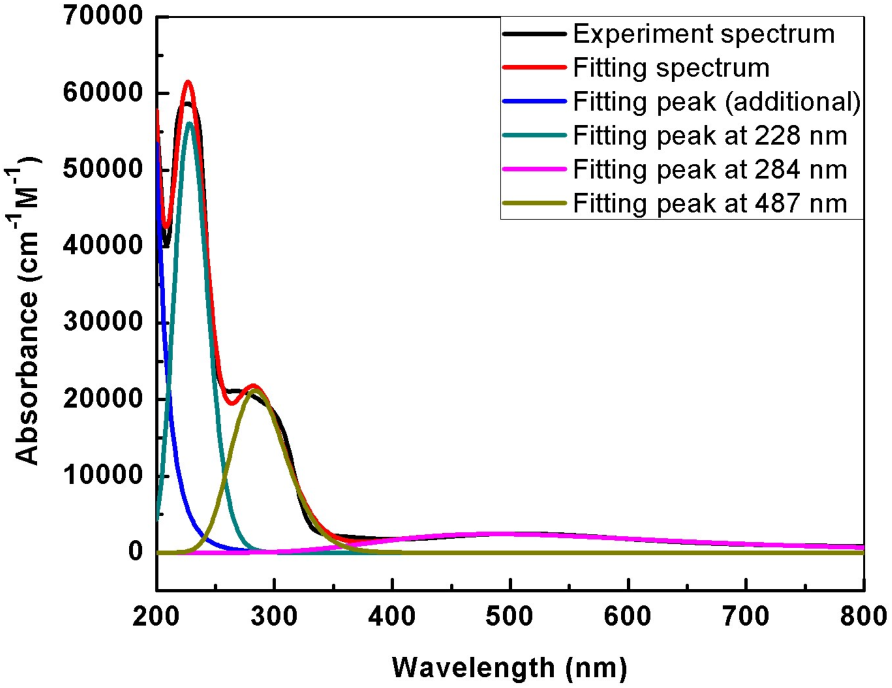

Figure S10. Gaussian fitting of the UV-Vis spectrum of [Ce(H_2A)$_3$]Cl in H_2O. (Fitting by energy and plotting by wavelength)

X-ray absorption spectroscopy

Ce L_{III}-edge XANES data were collected at the Stanford Synchrotron Radiation Lightsource, Beamline 11-2, using a Si 220 ($\varphi = 0$) double monochromator that was detuned to 20% and a Rh-coated harmonic rejection mirror with a cutoff energy set near 10 keV in order to reduce harmonic contamination. The resulting data have an energy resolution limited by the broadening due to the $2p_{3/2}$ core hole lifetime of 3.2 eV. Data were collected in transmission, using a CeO_2 reference to calibrate the energy scale, setting the first inflection point of the CeO_2 absorption to 5723 eV. A linear pre-edge background was subtracted, and the data were subsequently normalized to unity.

The samples were prepared for these experiments using procedures outlined previously.[8] Though the compound is air stable, it was prepared in a drybox for convenience. The sample was ground into a powder, mixed with dry boron nitride as a diluent, and then packed into the slots of a machined aluminum sample holder in an Ar atmosphere drybox. Aluminized mylar was affixed to the holder with an indium-wire seal. After packaging, the samples were transported in dry, argon-filled containers to the beamline. Sample holders were quickly transferred to the vacuum chamber, exposing the sealed holders to air for less than 30 seconds before pumping out the chamber and collecting the data under vacuum.

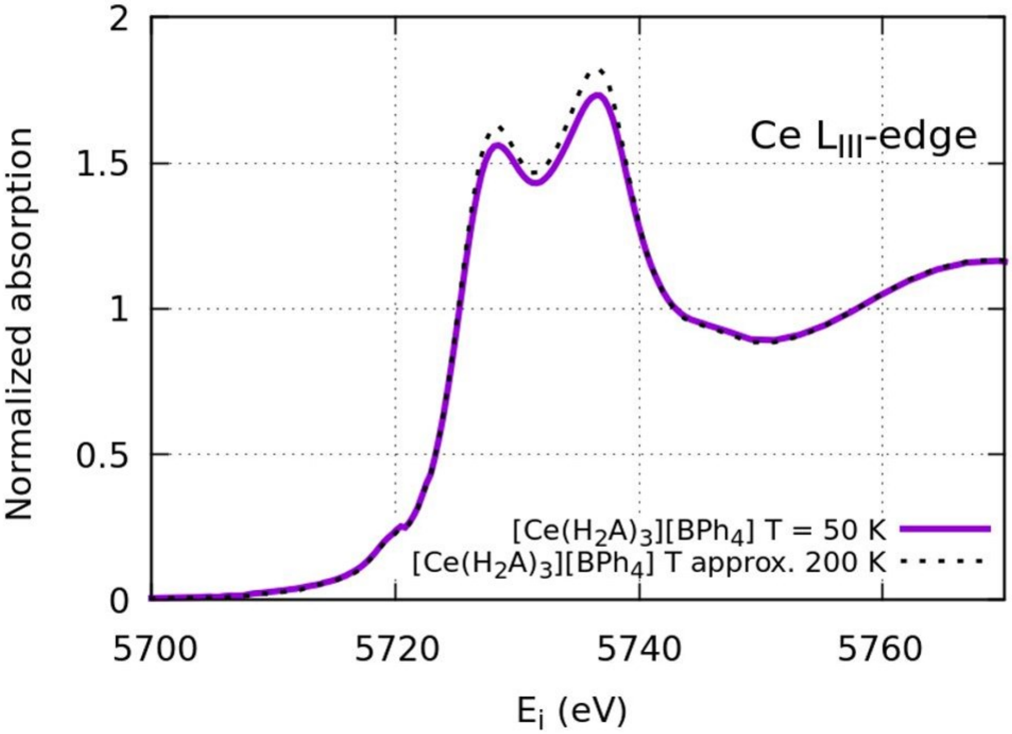

Figure S11. X-ray absorption spectrum of $[Ce(H_2A)_3][BPh_4]$ crystal. The spectrum at 50 K exhibits the double-peak feature expected for cerium (IV). No temperature-dependent changes were observed upon raising the temperature to approximately 200 K.

XANES fitting methods

XANES data were fit to extract n_f according to previously described methods.[8-10] The fits consisted of a sum of a step-like function to model the absorption edge and two Gaussians to fit peaks associated with f^1 and f^0 configurations, in addition to a third Gaussian was fit to the pre-edge peak at around 5720 eV and a fourth Gaussian which was fit to account for the EXAFS region. The step-like function (integrated Gaussian) models excitations into the continuum whose position is given by a weighted average of the f^1 and f^0 peak energies, rather than using two step-like functions, to reduce the number of parameters in the fit and control correlations between fitting parameters. This edge step is defined according to the expression:

$$I_{edge}(E) = \int_{-\infty}^{E} C_{edge} e^{\frac{-\left(E' - E_0\right)^2}{2\sigma^2}} dE',$$

and the Gaussians defined according to the expression:

$$I_i(E) = \frac{A_i}{\sqrt{2\pi}\sigma_i} e^{\frac{-\left(E - e_i\right)^2}{2\sigma_i^2}},$$

where E is the incident energy, e_i is the peak energy, σ_i is the half-width of the Gaussian and I_i is the intensity of peak i. E_0 is constrained to be the average of the peak energies of f^1 and f^0 weighted by the area under each associated Gaussian, A_i. The fractional f-occupancy n_f is calculated via:

$$n_f = \frac{A_{III}}{A_{III} + A_{IV}},$$

where A_{III} and A_{IV} are the areas for the expected Ce(III) and Ce(IV) features in the spectra. Error bars on calculated n_f values determined from the ratio of f^1 and f^0 peak areas are estimated to be about 0.03 normalized units.

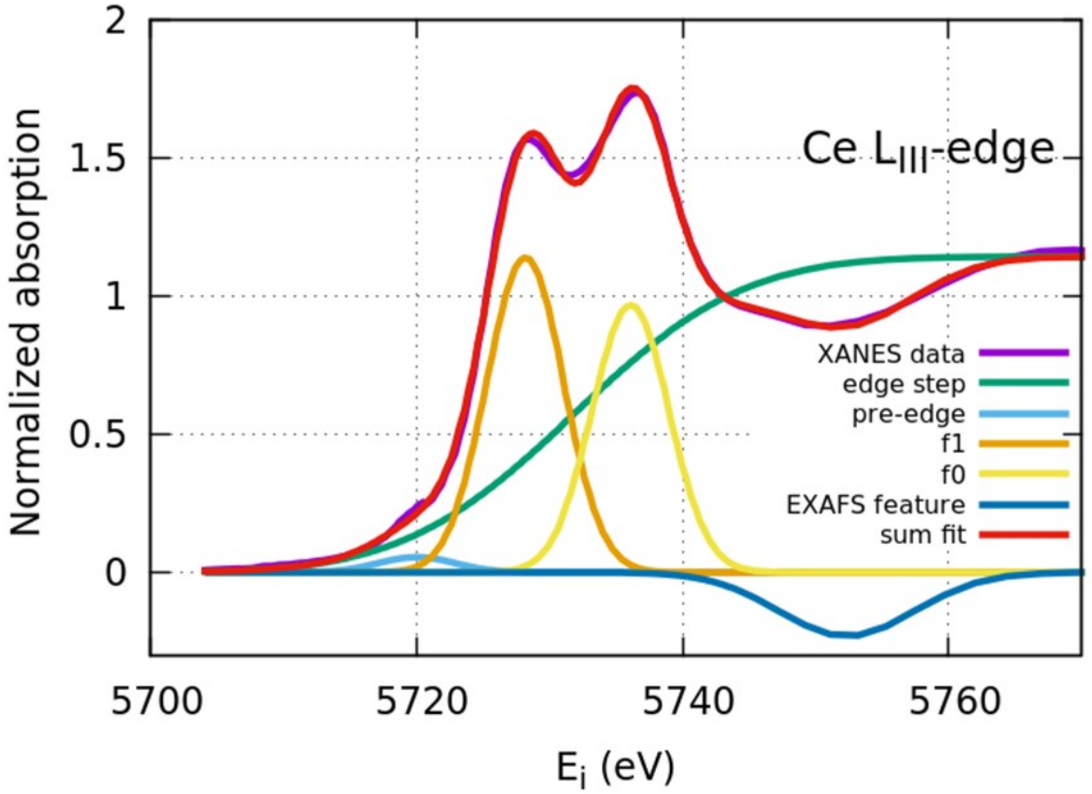

Figure S12. Fit of XANES data for $[Ce(H_2A)_3][BPh_4]$ sample.

Table S2. Fit parameter results for f^1 and f^0 integrated peak areas. Error estimates are determined from the covariance matrix and data errors determined by assuming the fitted χ^2 parameter equals the degrees of freedom in the fit. These peak areas were used to calculate n_f, which was found to be 0.54(3).

Sample	f^1 peak area	f^0 peak area	R(%) from Fit
$[Ce(H_2A)_3][BPh_4]$	8.3(1)	7.00(9)	1.75

Electrochemistry data

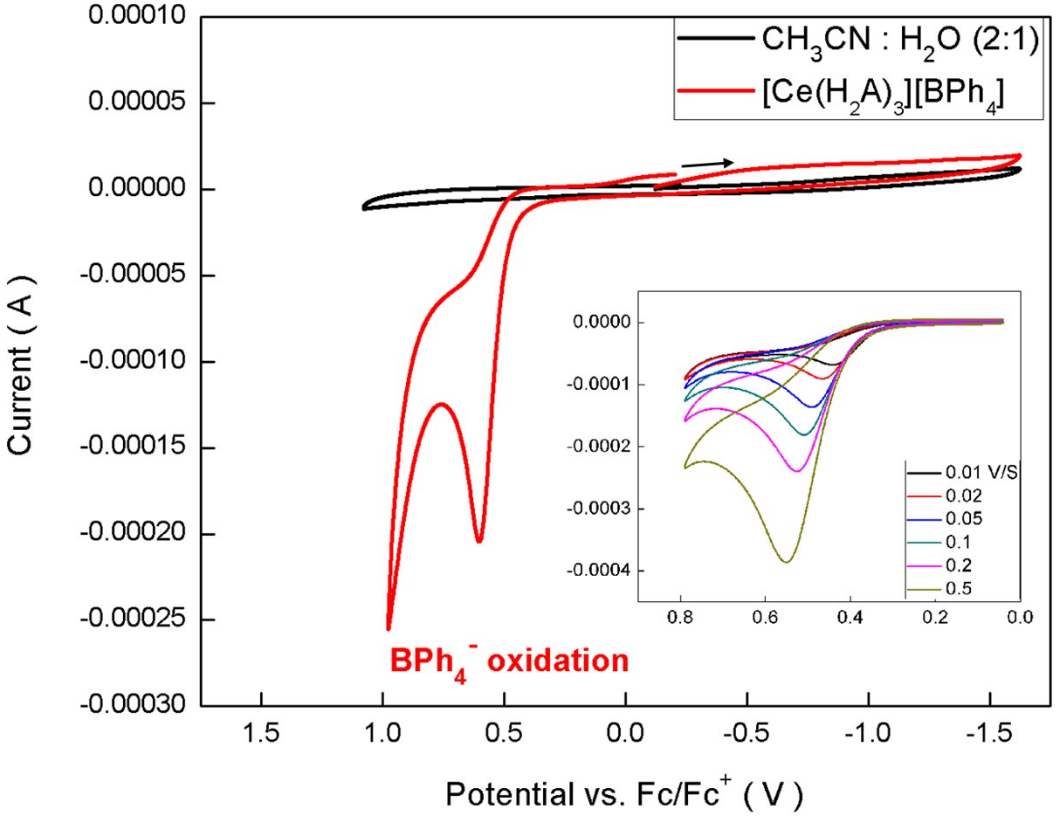

Figure S13. Cyclic voltammograms of [Ce(H_2A)$_3$][BPh$_4$] (2 mM) dissolved in CH_3CN:H_2O (4:1, v/v) The red peak corresponds to BPh$_4^-$ oxidation. The rate dependent scan corresponds to BPh$_4^-$ oxidation. The black arrow indicates the direction of the scan. Tetrabutylammonium hexafluorophosphate (TBAPF$_6$, 0.1 M) was used as an electrolyte.

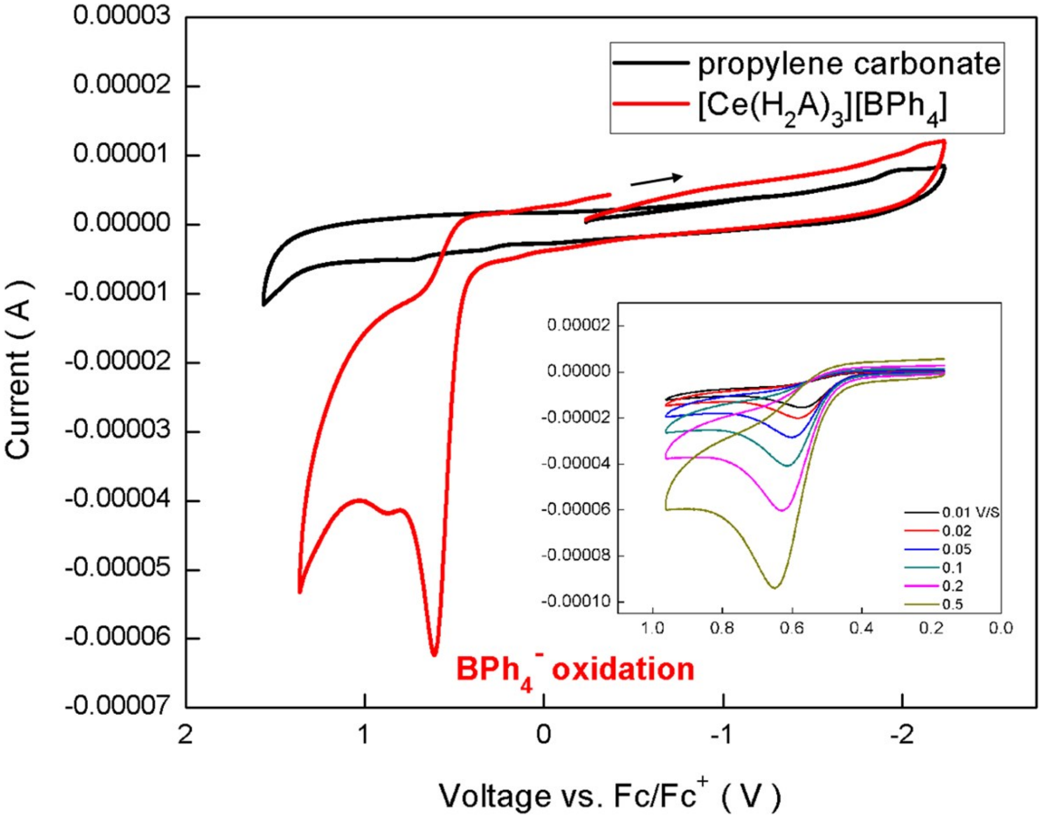

Figure S14. Cyclic voltammograms of [Ce(H$_2$A)$_3$][BPh$_4$] (2 mM) dissolved in propylene carbonate. The peak corresponds to BPh$_4^-$ oxidation. The rate dependent scan corresponds to BPh$_4^-$ oxidation. The black arrow indicates the direction of the scan. Tetrabutylammonium hexafluorophosphate (TBAPF$_6$, 0.1 M) was used as an electrolyte.

Computational data

First DFT calculation

In the first calculation, the geometry is optimized by cam-b3lyp-d3bj as functional, ECP28MWB genecp and 6-311+G* as basis set for cerium and other atoms, H_2O CPCM as solvent continuum, and the cation of $[Ce(H_2A)_3]Cl$ in the crystal structure as starting geometry. This calculation method has been used for H_3A and Mn in previous report.[11]

Table S3. Comparison of experimental and calculated metrical parameters.

Species	**$[Ce(H_2A)_3]Cl$**	**$[Ce(H_2A)_3][BPh_4]$**	**$[Ce(H_2A)_3]^+$ calculated structure**
Ce-O	2.369(4)-2.404(4)	2.3581(10)-2.4157(10)	2.38-2.39
Ce-N	2.470(6)-2.487(5)	2.4774(12)-2.4899(12)	2.53-2.53
O-N	1.367(6)-1.377(6)	1.3575(15)-1.3733(15)	1.34-1.34
C-N	1.343(6)-1.353(7)	1.3471(19)-1.3542(18)	1.34-1.34
C=N	1.295(7)-1.302(7)	1.2968(19)-1.302(2)	1.30

Table S4. Ligand and cerium 4f contribution to selected orbitals in the first DFT calculation using AOMix program.[12-13]

Orbitals	**Ligand composition (%)**	**Ce 4-f composition (%)**
HOMO-4	98.04	1.73
HOMO-3	98.14	1.62
HOMO-2	95.65	2.58
HOMO-1	95.87	2.47
HOMO	98.86	2.24
LUMO	2.35	97.64
LUMO+1	4.65	95.34
LUMO+2	4.34	95.25
LUMO+3	6.57	92.59
LUMO+4	3.84	95.78

LUMO+5	6.68	92.79
LUMO+6	6.65	92.85
LUMO+7	93.29	2.22
LUMO+8	97.66	1.32

TD-DFT calculation

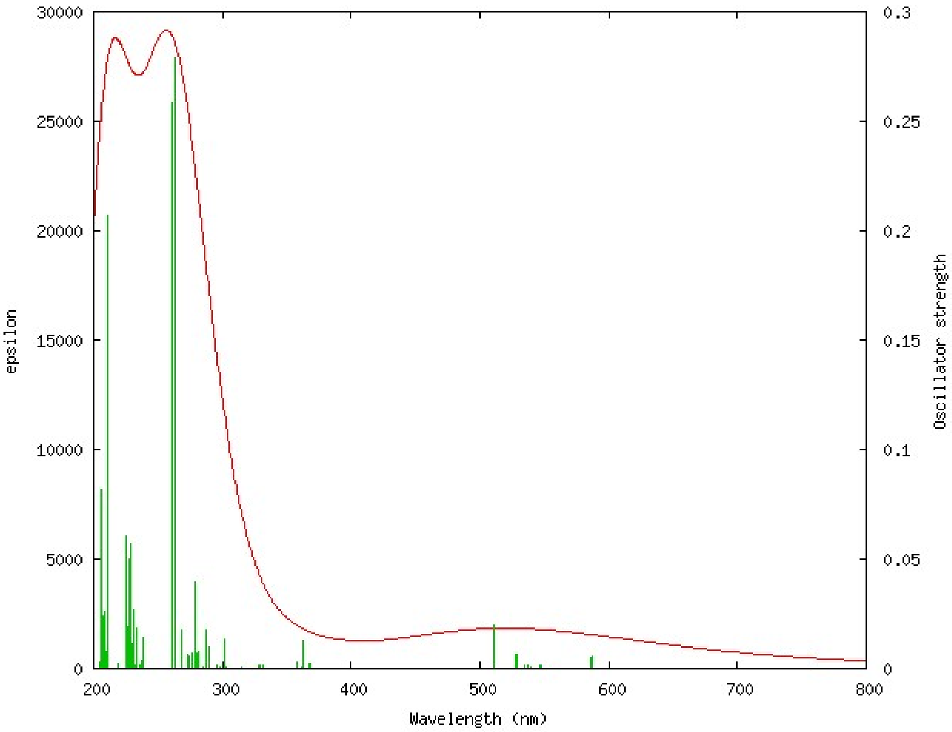

Figure S15. Predicted electron transition bands. (The predicted UV-Vis spectrum was made by oscillator strength from TD-DFT calculation and FWHM at 8000 cm-1. TD-DFT calculation was based on DFT calculation from table S1, Iop(8/11=1) and Nstates=150. FWHM stands for full width at half maximum.)

Table S5. Major electronic transitions predicted by TD-DFT and their principal molecular orbital component.

Electron transition bands (nm)	**Molecular component**		
510.5	H-2->L+6 (32%)	H-1->L+5 (26%)	H-1->L+1 (16%)
510.5	H-2->L+5 (34%)	H-1->L+6 (30%)	
263.9	HOMO->L+7 (48%)		
261.1	H-1->L+7 (25%)	HOMO->L+9 (16%)	
261.0	H-2->L+7 (24%)	HOMO->L+8 (16%)	
210.8	H-4->L+7 (35%)	H-16->L+1 (12%)	
210.7	H-3->L+7 (31%)	H-15->L+1 (16%)	

Second DFT calculation for comparison

A second DFT calculation method used B3LYP as the functional, ECP28MWB genecp and 6-31G* as basis set for cerium and other atoms, CH_2Cl_2 CPCM as solvent continuum, and the crystal structure as starting geometry. This method has been used for the prediction of reduction potential in a varieties of cerium complexes.[14]

In comparison, the first method has used cam-B3LYP-d3 as functional other than B3LYP because the electrons on ligands are more delocalized. This method has been used by Xiang Xie in H_3A related calculation. Cam-B3LYP-d3 is a range-corrected and diffuse electron method, which is more suitable for the geometry optimization for $[Ce(H_2A)_3]^+$ system.

Here we compared the bond distance/length as the criteria for the priority of calculation. The result showed that the first calculation gave more accurate result than the second one with 0.02 Å closer for Ce-O bond length and 0.03 Å more accurate for Ce-N bond length.

Table S6. Comparison of experimental and calculated metrical parameters.

Species	$[Ce(H_2A)_3]Cl$	$[Ce(H_2A)_3][BPh_4]$	$[Ce(H_2A)_3]^+$ 1st calc. (cam-b3lyp-d3)	$[Ce(H_2A)_3]^+$ 2nd calc. (b3lyp)	
Ce-O	**2.369(4)-2.404(4)**	**2.3581(10)-2.4157(10)**	**2.38-2.39**	**2.40-**	**2.40**
Ce-N	**2.470(6)-2.487(5)**	**2.4774(12)-2.4899(12)**	**2.53-2.53**	**2.56-**	**2.56**
O-N	1.367(6)-1.377(6)	1.3575(15)-1.3733(15)	1.34-1.34	1.34-	1.34
C-N	1.343(6)-1.353(7)	1.3471(19)-1.3542(18)	1.34-1.34	1.34-	1.34
C=N	1.295(7)-1.302(7)	1.2968(19)-1.302(2)	1.30	1.31	

The calculated electronic transitions from TD-DFT have been compared to the UV-Vis spectrum as well. The first method gave transitions at 228, 284, 487 nm; the second method gave transitions at 440, 644 nm; the UV-Vis spectrum gave absorption peaks at 228, 284, 487 nm. Therefore, the first calculation gave better result.

The IR spectra predicted by the two different methods were similar to each other, with small differences in energy. The real IR spectrum is quite different due to H_2O.

Second DFT calculation for predicted reduction potential

The second DFT calculation was not the best for geometry optimization, but was commonly used for reduction potential prediction.[9] The calculation of $[Ce^{IV}(H_2A)_3]^+$ and $[Ce^{III}(H_2A)_3]$ was carried out with b3lyp functional, genecp basis set with ECP28MWB for cerium and 6-31G* for other atoms, CH_2Cl_2 CPCM as solvent continuum, and crystal structure as starting geometry. Total energy difference between cerium III/IV complexes was transferred into voltage unit and then calibrated to the corrected predicted $E^{1/2}$, which was -1.22 V. This value was quite negative and showed that the ligand could potentially stabilize cerium +4 oxidation states.

Table S7. Predicted reduction potential of cerium III/IV. E1/2 DCM was calculated (Ar = 2,6-diphenylphenol, OEP=octaethylporphyrin).

Compounds	Ce^{3+} G (Hartrees)	Ce^{4+} (Hartrees)	dG DCM (eV)	$E_{1/2}$ DCM (V vs Fc)	$E_{1/2}$ DCM corrected (V vs Fc)	Experimental (V vs Fc)
$[Ce(H_2A)_3]^+$	-2005.29	-2005.15	-3.78	-1.46	**-1.22**	\
$Ce(OAr)_4$	-3550.52	-3550.36	-4.42	-0.83	-0.59	-0.50
$Ce(OEP)_2$	-2451.68	-2451.53	-4.18	-1.06	-0.82	-1.06

Reference:

1. Bruker, SHELXTL. Bruker AXS Inc.: Madison, Wisconsin, USA, 2009.; SAINT v8.38A: Bruker-AXS Madison, Wisconsin, USA (2014).
2. SADABS v2016/2: Krause, L., Herbst-Irmer, R., Sheldrick, G.M. & Stalke, D., J. Appl. Cryst., 2015, **48**, 3-10.
3. Sheldrick, G. M., TWINABS. University of Gottingen, Germany, 2008.
4. G. M. Sheldrick, Crystallographic shelves: space-group hierarchy explained, *Acta Cryst.,* A, 2015, **71,** 3-8.
5. Frisch, M. J.; Trucks, G. W.; Schlegel, H. B.; Scuseria, G. E.; Robb, M. A.; Cheeseman, J. R.; Scalmani, G.; Barone, V.; Mennucci, B.; Petersson, G. A.; Nakatsuji, H.; Caricato, M.; Li, X.; Hratchian, H. P.; Izmaylov, A. F.; Bloino, J.; Zheng, G.; Sonnenberg, J. L.; Hada, M.; Ehara, M.; Toyota, K.; Fukuda, R.; Hasegawa, J.; Ishida, M.; Nakajima, T.; Honda, Y.; Kitao, O.; Nakai, H.; Vreven, T.; Montgomery, J. A.; Peralta, J. E.; Ogliaro, F.; S64 Bearpark, M.; Heyd, J. J.; Brothers, E.; Kudin, K. N.; Staroverov, V. N.; Kobayashi, R.; Normand, J.; Raghavachari, K.; Rendell, A.; Burant, J. C.; Iyengar, S. S.; Tomasi, J.; Cossi, M.; Rega, N.; Millam, J. M.; Klene, M.; Knox, J. E.; Cross, J. B.; Bakken, V.; Adamo, C.; Jaramillo, J.; Gomperts, R.; Stratmann, R. E.; Yazyev, O.; Austin, A. J.; Cammi, R.; Pomelli, C.; Ochterski, J. W.; Martin, R. L.; Morokuma, K.; Zakrzewski, V. G.; Voth, G. A.; Salvador, P.; Dannenberg, J. J.; Dapprich, S.; Daniels, A. D.; Farkas, O.; Foresman, J. B.; Ortiz, J. V.; Cioslowski, J.; Fox, D. J. Gaussian 09, Revision A.02; Gaussian, Inc.: Wallingford, CT, 2009.
6. Z. Zhang, B. F. Parker, T. D. Lohrey, S. J. Teat, J. Arnold and L. Rao, Complexation-assisted reduction: complexes of glutaroimide-dioxime with tetravalent actinides (Np(IV) and Th(IV)), *Dalton Trans.,* 2018, **47,** 8134–8141.
7. L. Xian, G. Tian, C. M. Beavers, S. J. Teat and D. K. Shuh, Glutarimidedioxime: A complexing and reducing reagent for plutonium recovery from spent nuclear fuel reprocessing, *Angew. Chem. Int. Ed.,* 2016, **55,** 4671-4673.
8. C. H. Booth, M. D. Walter, D. Kazhdan, Y. J. Hu, W. W. Lukens, E. D. Bauer, L. Maron, O. Eisenstein, R. A. Andersen, Decamethylytterbocene complexes of bipyridines and diazabutadienes: multiconfigurational ground states and open-shell singlet formation, *J. Am. Chem. Soc.* 2009, **131,** 6480−6491.
9. C. H. Booth, D. Kazhdan, E. L. Werkema, M. D. Walter, W. W Lukens, E. D. Bauer, Y. J. Hu, L. Maron, O. Eisenstein, Head-Gordon, R. A. Andersen, Intermediate-valence tautomerism in decamethylytterbocene complexes of methyl-substituted bipyridines, *J. Am. Chem. Soc.* 2010, ***132***, 17537-17549
10. R. L. Halbach, G. Nocton, C. H. Booth, L, Maron, R. A. Andersen, Cerium tetrakis(tropolonate) and cerium tetrakis(acetylacetonate) are not diamagnetic but Ttemperature-independent paramagnets, *Inorg. Chem.,* 2018, ***57*** (12), 7290-7298.
11. X. Xie, Y. Tian, Z. Qin, Q. Yu, H. Wei, D. Wang and X. Li, X. Wang, Complexation of manganese with glutarimidedioxime: Implication for extraction uranium from seawater, *Sci. Rep.,* 2017, **7,** 43503.
12. S. I. Gorelsky, AOMix: Program for Molecular Orbital Analysis; version 6.90, 2017, http://www.sg-chem.net/
13. 1 S. I. Gorelsky, A. B. P. Lever, Electronic structure and spectra of ruthenium diimine complexes by density functional theory and INDO/S. Comparison of the two methods, *J. Organomet. Chem.,* 2001, **635,** 187-196.

14. J. A. Bogart, A. J. Lewis, M. A. Boreen, H. B. Lee, S. A. Medling, P. J. Carroll, C. H. Booth and E. J. Schelter, A ligand field series for the 4f-Block from experimental and DFT computed Ce(IV/III) electrochemical potentials, *Inorg. Chem.,* 2015, **54,** 2830-2837.